Journal of Neuroscience Methods 403 (2024) 110039

Contents lists available at ScienceDirect

Journal of Neuroscience Methods

journal homepage: www.elsevier.com/locate/jneumeth

Detectability and accuracy of computational measurements of *in-silico* and physical representations of enlarged perivascular spaces from magnetic resonance images

Roberto Duarte Coello [a], Maria del C. Valdés Hernández [a,*], Jaco J.M. Zwanenburg [b], Moniek van der Velden [b], Hugo J. Kuijf [b], Alberto De Luca [b], José Bernal Moyano [a,c,d], Lucia Ballerini [a,e], Francesca M. Chappell [a], Rosalind Brown [a], Geert Jan Biessels [b], Joanna M. Wardlaw [a]

[a] Centre for Clinical Brain Sciences, Department of Neuroimaging Sciences, University of Edinburgh, Edinburgh, UK
[b] Image Sciences Institute, UMC Utrecht, Utrecht, Netherlands
[c] German Centre for Neurodegenerative Diseases, Magdeburg, Germany
[d] Institute of Cognitive Neurology and Dementia Research, Otto-von-Guericke University Magdeburg, Magdeburg, Germany
[e] University for Foreigner of Perugia, Perugia, Italy

ARTICLE INFO

Keywords:
Perivascular spaces
Virchow-Robin spaces
MRI phantom

ABSTRACT

Background: Magnetic Resonance Imaging (MRI) visible perivascular spaces (PVS) have been associated with age, decline in cognitive abilities, interrupted sleep, and markers of small vessel disease. But the limits of validity of their quantification have not been established.
New method: We use a purpose-built digital reference object to construct an in-silico phantom for addressing this need, and validate it using a physical phantom. We use cylinders of different sizes as models for PVS. We also evaluate the influence of 'PVS' orientation, and different sets of parameters of the two vesselness filters that have been used for enhancing tubular structures, namely Frangi and RORPO filters, in the measurements' accuracy.
Results: PVS measurements in MRI are only a proxy of their true dimensions, as the boundaries of their representation are consistently overestimated. The success in the use of the Frangi filter relies on a careful tuning of several parameters. Alpha= 0.5, beta= 0.5 and c= 500 yielded the best results. RORPO does not have these requirements and allows detecting smaller cylinders in their entirety more consistently in the absence of noise and confounding artefacts. The Frangi filter seems to be best suited for voxel sizes equal or larger than 0.4 mm-isotropic and cylinders larger than 1 mm diameter and 2 mm length. 'PVS' orientation did not affect measurements in data with isotropic voxels.
Comparison with existent methods: Does not apply.
Conclusions: The in-silico and physical phantoms presented are useful for establishing the validity of quantification methods of tubular small structures.

1. Introduction

Perivascular spaces (PVS), eponymously named Virchow-Robin spaces after the 19th-century anatomists and pathologists Rudolf Virchow and Charles Philippe Robin, are fluid-filled spaces that surround the walls of the blood vessels. PVS in the brain have attracted the attention from the scientific community due to their suspected role in waste clearance and thus their potential value as an imaging biomarker of brain health function (Wardlaw et al., 2020; Donahue et al., 2021; Sepehrband et al., 2021). Their increase in size to diameters from 1 to 3 mm and lengths from 3 to 5 mm (Valdés Hernández et al., 2013), prompting their visibility in magnetic resonance images (MRI), has been associated with cognitive dysfunction in the elderly (Hilal et al., 2018; Passiak et al., 2019) possibly even more strongly than other markers of small vessel disease (Passiak et al., 2019), sleep dysfunction (Aribisala et al., 2020; Baril et al., 2022; Berezuk et al., 2015; Del Brutto et al., 2019), inflammatory markers (Aribisala et al., 2014), hypertension (Dubost et al., 2019), ageing, brain lacunes, and microbleeds (Francis

* Correspondence to: Centre for Clinical Brain Sciences, Chancellor's Building, 49 Little France Crescent, Edinburgh EH16 4SB, UK.
E-mail address: M.Valdes-Hernan@ed.ac.uk (M.C. Valdés Hernández).

https://doi.org/10.1016/j.jneumeth.2023.110039
Received 25 July 2023; Received in revised form 27 November 2023; Accepted 17 December 2023
Available online 20 December 2023

et al., 2019). PVS burden has also been associated with the speed of white matter deterioration in older adults, and partially mediating the effect of sleep in white matter health (Aribisala et al., 2023). It is therefore not surprising that several methods for assessing PVS from magnetic resonance images (MRI) have been developed, ranging from visual scoring systems (Patankar et al., 2005; Potter et al., 2015) to fully-automated computational approaches (Pham et al., 2022; Barisano et al., 2022).

While neuroradiological scoring has been largely considered the reference standard, advances in scientific and research methodologies have made large-scale research a norm. Large databases that combine clinical, demographic, genetic and imaging data (e.g., https://imaging.cancer.gov/informatics/cancer_imaging_archive.htm) are rapidly emerging to underpin and advance clinical research, but they are only partially annotated, and expert visual assessment at such scale is implausible. Also, due to the nature (i.e., void spaces once dissected) and size of this features (i.e., wide range in microscopic scale) and post-mortem tissue collapse, comparison of in-vivo MRI measurements with histology will be imprecise. Automatic methods to assess brain enlarged PVS would enable analyses of very large studies. However, they have been evaluated against neuroradiological ratings and manually-annotated images in only one slice per region of interest or in only few cases (Pham et al., 2022). Moreover, the limits of validity of these techniques and accuracy levels in measuring PVS are still not known. MRI from the human brain alone is unlikely to provide this information as measurements of small brain structures are compromised by image resolution, confounding pathologies, and artefactual effects, the CSF pulsation due to the heartbeat being one of them. Previous study presented a Digital Reference Object (DRO) designed for this purpose (Bernal et al., 2022) and evaluated the performance of three image enhancement methods under various spatiotemporal imaging considerations including sampling, motion artefacts, and Rician noise. We here use this previously developed DRO as part of an *in-silico* phantom, and use it together with a physical phantom to inform on a) the influence of the choice of filter parameters in the measurements b) how the spatial resolution of the image influences the PVS diameter measured, c) the influence of PVS orientation in the accuracy of the measurements, d) the differences introduced by the choice of filtering methods (in absence of noise and confounding artefacts), and e) the detectability of PVS in research protocols using MRI scans with 1 mm^3 isotropic voxels.

2. Materials and methods

2.1. PVS DRO

PVS are seen in MRI as thin linear or small punctate structures depending on the visualisation axis, with signal intensity similar to that of CSF (Valdés Hernández et al., 2013; Wardlaw et al., 2013). Using this description, Bernal et al. (2022) choose a cylinder as a geometric model of PVS. The parametric equation of a cylinder is given by:

$$\frac{d^2}{4} \geq x^2 + y^2, \tag{1}$$

for $-l/2 \leq z \leq l/2$, where x, y and z are the 3D coordinates, l is the cylinder length and d is the diameter of the cylinder. The volume of the cylinder is calculated using

$$v = \pi l \frac{d^2}{4}. \tag{2}$$

2.2. In-silico phantom

We define our PVS binary mask (1: if the voxel is inside the cylinder; and 0: otherwise) using Eq. (1) and consider it a PVS representation in high resolution. We, then, reduce the resolution using a linear interpolation to simulate PVS in a lower-resolved image and introduce partial volume effects. The intensity of the voxel in a given coordinate (x,y,z) of the image space is then modelled via the following equation:

$$f(x,y,z) = M(x,y,z)(1 - P(x,y,z)) + aP(x,y,z), \tag{3}$$

where M is the intensity of the background (usually white matter intensity), P is the proportion of PVS in the voxel (i.e., the full PVS "body" or a border with partial volume), and a is the intensity of the CSF in the scan (i.e., equal to the intensity of the simulated PVS).

We generate several "PVS" in our *in-silico* phantom by varying the diameter, length and orientation of the cylinders. In particular, we vary the diameter from 0.2 to 3 mm, the length from 1.02 to 13 mm, and we rotate the cylinders around the x-axis from 0° to 180° and the z-axis from −45° to 45°. We confine each cylinder within a space of $15 \times 15 \times 15$ mm^3 as per maximum length definition (Valdés Hernández et al., 2013; Wardlaw et al., 2013), and to avoid them being too close to each other. We constructed our *in-silico* PVS phantom by placing together all the cubes of $15 \times 15 \times 15$ mm^3, as can be seen in Fig. 2.

2.3. UMC Utrecht PVS phantom

We analysed images from a physical phantom built at the Utrecht University Medical Centre with the primary purpose of investigating the influence of spatial resolution, orientation, and image analysis method, on the accuracy of measurements of PVS in a 7 T MRI scan, in parallel to validate our *in-silico* phantom. The UMC Utrecht PVS phantom consists of a Perspex plate with holes of diameters ranging from 0.2 to 3 mm, filled with water, and scanned with a T2-weighted contrast using a turbo spin-echo sequence in a 7 T MRI scanner (Fig. 4). Water-filled cylinders were checked to ensure absence of any curvature. The acquisition was similar to the acquisition used in previous work on imaging PVS in human volunteers (Bouvy et al., 2014), but slightly adjusted to the small phantom size, and adjusted to yield protocols for multiple isotropic resolutions. See Supplementary Table S1 for an overview of the scan parameters. Subsequently in this paper, we will mention the reconstructed voxel sizes while referring to the resolution of the images unless stated otherwise to facilitate the analyses and interpretation of the results. These are larger than the acquired voxel sizes. The acquisition resolution for each of the reconstructed images can be seen in Supplementary Table S1. In addition to the default orientations (i.e., coronal, sagittal and transverse), the field-of-view was also rotated 15°, 30°, and 45° around the 'feet-head' axis, which yields the most unfavourable positioning (i.e. these are rotations around an axis that is perpendicular to the centerlines of the holes).

Fig. 5 shows the images obtained. Holes of 0.2 and 0.3 mm diameters could not be filled with water. Therefore, they are not visible. Holes with diameters smaller than the voxel size are visible but attenuated due to partial volume effect. The PVS measured diameter in a scan depends on the location of the PVS relative to the voxel. Preferably, a PVS would run exactly through several voxels, but often it is located on the edge of two or various voxels or pass diagonally through a set of voxels. Here the holes representing PVS can appear enlarged as usually they are not aligned to the centre of the voxels they cross. The oblique length in the

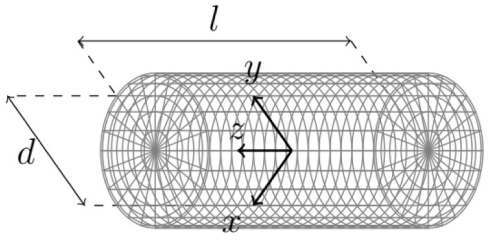

Fig. 1. Cylinder representing a linear PVS or a linear section of it, defined by Eq. (1) with length l and diameter d. The origin of the 3D space coordinates (x, y, z) to place this digital reference object is at the object's centre.

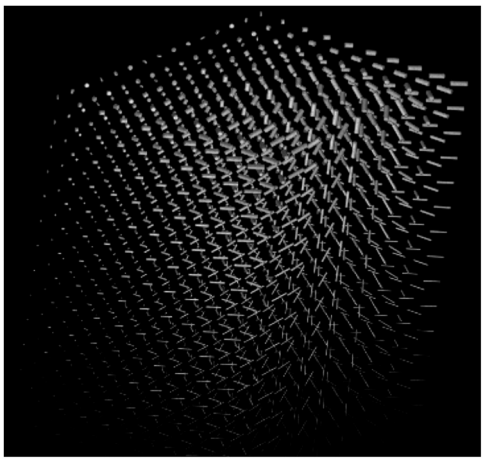

Fig. 2. *In-silico* PVS phantom constructed by placing together cubes of 15 x 15 x 15 mm^3, each containing a cylinder (i.e., DRO) with different widths, lengths and orientations.

plane (*l*2D) and the length of the body diagonal (l3D) can be calculated as the square root of the sum of squares of the voxel dimensions (i.e., l2D = sqrt(x^2 + x^2) and l3D = sqrt(x^2 + x^2 + x^2) for isotropic voxels of dimension x). In such way, for different settings, the lengths of the holes representing PVS can differ (see Supplementary Table S2).

2.4. Robustness of the physical phantom against geometric distortions

Geometric distortions induced mainly by the nonlinearities of the gradient field, enhanced by susceptibility differences at objects' boundaries (i.e., proportionate to the magnetic field strength, 7 T in this case) were present in the physical phantom as Fig. 4 shows. Although the central position of the fluid-filled cylinders assessed makes the impact of geometric distortions unlikely, we measured the geometric distortions using the method recommended by AAPM (Price et al., 1990) and the Institute of Physics and Engineering in Medicine in UK (Lerski et al., 1998; Wang and Doddrell, 2005) and compared the distances measured between the centres of the cylinders in the 2D orthogonal planes, with the correspondent ones in the phantom's design. Between adjacent cylinders no geometric distortions were found, and between the cylinders located at the extremes of the phantom, the geometric distortion was less than 0.8%.

2.5. Automatic PVS segmentation

We evaluate the performance of one of the fully-automated image processing/analysis methods most widely used in clinical research at present for segmenting PVS, which consists of enhancing PVS-like structures using a "vesselness" filter, thresholding the resulting "vesselness" likelihood map, and analysing the morphology of the segmented PVS. We evaluate two "vesselness" filtering methods, which are representative of the two classes of filters mostly used: 1) Hessian-based filters that rely on information provided by the Hessian matrix of the image, and 2) the morphological-based filters that rely on the mathematical morphology of the image intensities. We use the Hessian-based Frangi filter (Frangi et al., 1998), firstly used for PVS segmentation by Ballerini et al. (2018), and the morphological-based Ranking Orientation Responses of Path Operators (RORPO) (Merveille et al., 2018), firstly used for PVS segmentation by Bernal et al. (2022), which also evaluated the Jerman filter (Jerman et al., 2015). Looking at the results from Bernal et al. (2022) it can be noticed that the performance of Jerman and Frangi filters was very similar, but with Frangi always yielding better results. This, partly, is owed to the wider descriptive capabilities of the objects' geometry by Frangi (i.e., blobness, flatness and saliency) vs. those from Jerman (blobness only).

We explore the influence of the filter parameters in the segmentation, and further analyse the limits of validity and expectations of accuracy in the measurements of PVS-like structures using the optimal thresholds and the parameters previously published after these being validated in the corresponding pioneer publications. As such, for these analyses, the parameters of the Frangi filter were set as suggested in (Ballerini et al., 2016, 2018) $\alpha = 0.5, \beta = 0.5$ and $c = 500$, as we show in the analyses of the parameters of the Frangi filter that these values yield the best results. The scales of each filter were tuned for the image resolution. The intensities of each image were normalised to values from 0 to 255 only considering the region of interest (ROI). The filters were also applied to the images from the UMC Utrecht physical phantom. The optimum threshold applied to the resultant "vesselness" map was the one which allowed capturing holes across the whole (or most of the) range of diameters, and it was selected only on the image with the highest resolution and applied to the rest. The resulting segmentation mask was used to compute the results. Please note that we chose the threshold based on the physically acquired scans, because they have noise and artefacts that are not reflected in our *in-silico* phantom.

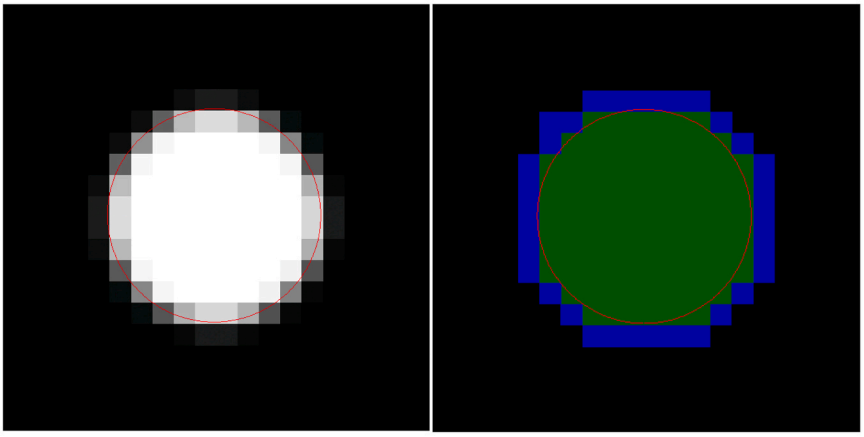

Fig. 3. Transversal cut of an example of PVS DRO with diameter 3 mm in isotropic voxels of 0.3 × 0.3 × 0.3 mm^3. (Left) Intensity image (Right) Segmentation mask. The red circle (i.e., thin perimeter line in the intensity image) indicates the true boundaries of the DRO, the green voxels are the voxels where the DRO occupies at least 30% of the voxels and the blue voxels are the surface of the DRO. The boundaries of the PVS representation, i.e., the measured dimensions, may be overestimated due to the partial volume effect (Fig. 3), as per Bernal et al. (2022).

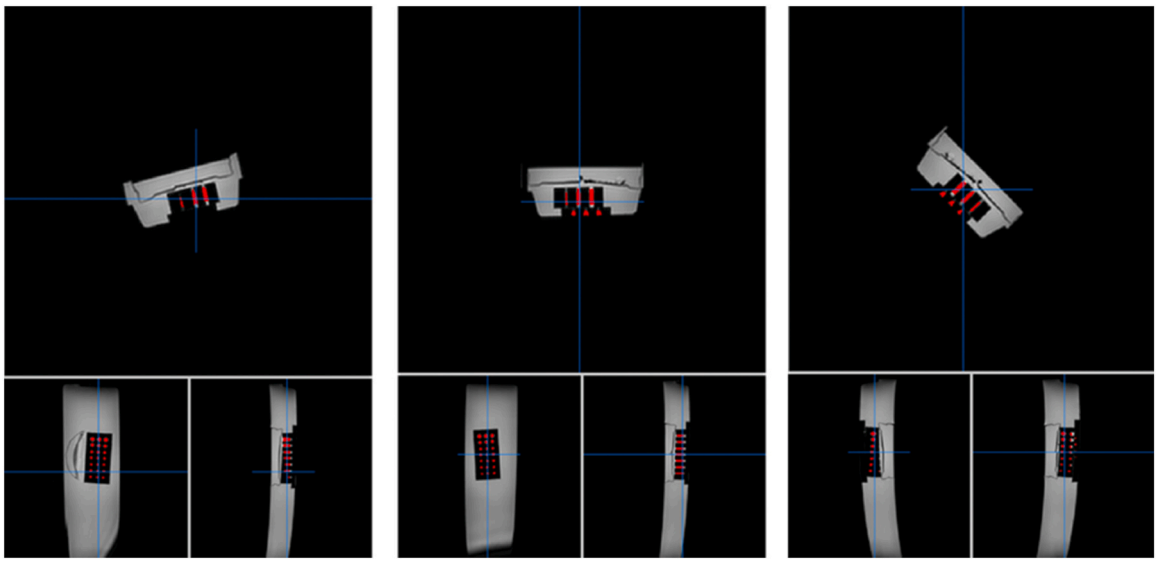

Fig. 4. UMC Utrecht physical phantom scanned in axial (transverse) orientation (i.e., R-L x A-P plane) with the field-of-view rotated at different angles. (Left) 15 degrees, (Centre) 0 degrees, (Right) 45 degrees.

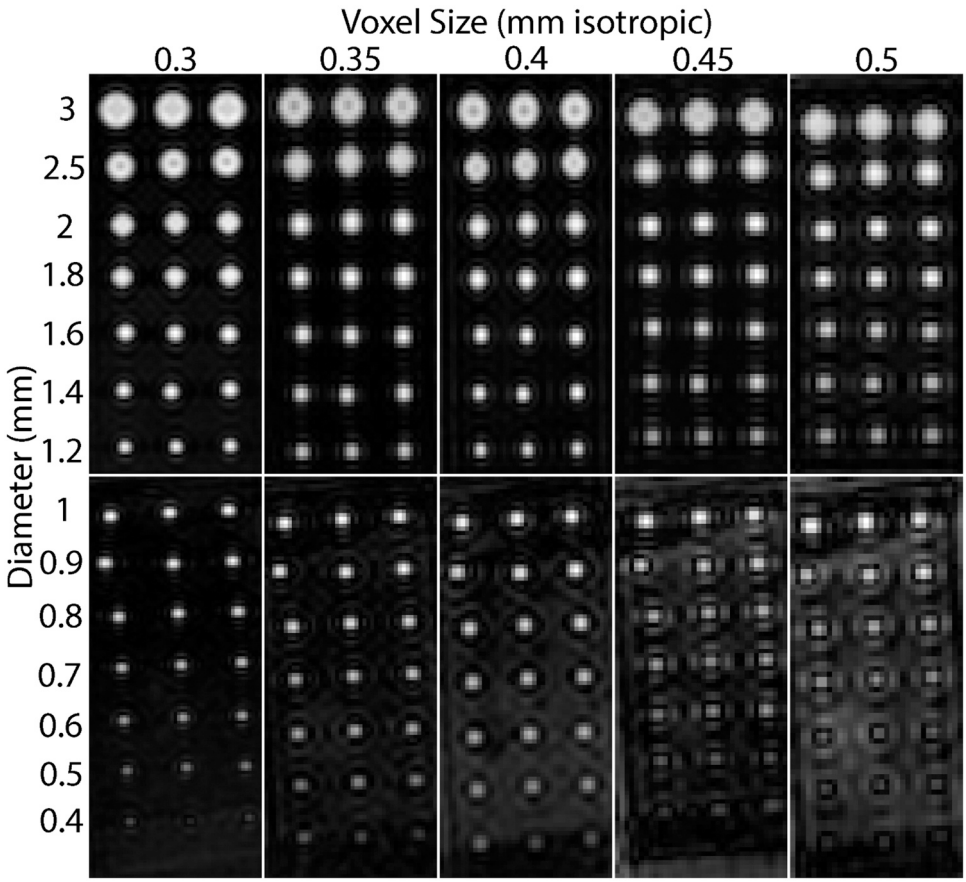

Fig. 5. Transversal slices from the UMC Utrecht phantom acquired with different resolutions. From left to right, reconstructed voxel sizes: 0.3, 0.35, 0.4, 0.45 and 0.5 mm-isotropic. (the acquired "physical" resolution was 0.6, 0.7, 0.8, 0.9 and 1.0 mm isotropic, respectively, see Suppl. Table S1). From top to bottom in upper panels hole diameters 3, 2.5, 2, 1.8, 1.6 and 1.2 mm; and 1, 0.9, 0.8, 0.7, 0.6, 0.5 and 0.4 mm in bottom panels. Please note that *k*-space ringing artefacts are more apparent with larger voxel sizes.

2.6. Image analyses

Using the *in-silico* phantom, we simulated the UMC Utrecht PVS (physical) phantom with voxel sizes varying from 0.3 to 0.5 mm (Supplementary Fig. S1), and calculated the diameters of the cylinders in both phantoms using the "PrincipalAxisLength" parameter from the MATLAB built-in function regionprops3. This function approximates an ellipsoid and returns the length of the principal axes. Since the objects

are straight, it is a good approximation for the dimensions of a cylinder. We use the highest value as length and the second largest as diameter. We plotted the segmentation and the results obtained from each filtering method for each phantom (i.e., *in-silico* and physical) to illustrate the expectations in accuracy of the PVS segmentation in absence of noise and confounding artefacts for each spatial resolution, and to evaluate the fidelity with which our *in-silico* phantom can be used to represent a physical MRI phantom for evaluating the accuracy of PVS segmentations. We also analysed the impact of PVS orientation in the measurement accuracy at voxel sizes of $0.35 \times 0.35 \times 0.35\ mm^3$ in both phantoms. We further analysed the limits of validity of the computational measurements that use the two filtering methods evaluated, in images with 1 mm-isotropic voxels, as this is the spatial resolution commonly used in medical research imaging protocols. For this, in our *in-silico* phantom, we generated cylinders from 0.1–3 mm diameter and from 0.1–10 mm length with different orientations and plotted the results. If at least 1 voxel inside a cylinder could be identified, then it was considered as detected. Otherwise, it was considered as not detected.

2.7. Statistical analyses

Differences between all the cylinder diameters' measurements at each voxel size were investigated using box plots. The average measurements, range, and absolute differences from the real measurements (i.e., ideal values, physically measured using a hole gage and a calliper in the physical phantom, or derived from the cylinder equation in the in-silico phantom) of the cylinders obtained from using each filtering method were compared using the paired Wilcoxon sign rank test. Bland-Altman analyses of the diameters' measurements were also performed, but excluding the undetected cylinders (i.e., those for which the measurement diameter equalled zero).

2.8. Data availability statement

The data and source code correspondent to the analyses contained in this manuscript are publicly available from https://doi.org/10.7488/ds/7454.

3. Results

3.1. Accuracy of the PVS measurements at different spatial resolutions

Fig. 6 shows the results from measuring the diameter of the cylinders of both phantoms at spatial voxel sizes of 0.3, 0.4 and 0.5 mm-isotropic, and Fig. 7 shows the Bland-Altman plots of the differences between the average diameter measurements from both filters and the ideal cylinder diameters at voxel sizes of 0.3, 0.35, 0.4, 0.45, and 0.5 mm-isotropic (see also Supplementary Fig. S2). The RORPO filter had increased sensitivity compared to the Frangi filter for detecting small cylinders, between 0.5 and 2.0 mm diameters regardless of the voxel size, while the Frangi filter yielded better results when measuring diameters higher than 1.0 mm for voxels equal or bigger than 0.45 mm-isotropic (i.e., from the ones evaluated in these experiments) (See Supplementary Table S5). Measurements obtained using RORPO showed a linear correspondence between the measured diameter and the real diameter (i.e., ideal value) across the range of diameters evaluated. For smaller voxel sizes (i.e., 0.3 and 0.4 mm-isotropic), diameter measurements were closer to the ideal segmentation of the *in-silico* phantom considering all voxels of the cylinders (i.e., including those with partial volume effects), while for voxel sizes of 0.5 mm-isotropic, they were closer to the ideal segmentation of the in-silico phantom considering voxels located at least 30% inside the cylinders (e.g., green masked area in Fig. 3 right panel). Deviations from the ideal measurements, e.g. non-uniformities of the filter output inside the objects, were also observed. The measured diameters in both (i.e., *in-silico* and physical) phantoms followed similar pattern across sizes when compared to the theoretical values, in addition of being close to each other, thus providing confidence in the use of our in-silico phantom model to establish the limits of validity of the PVS segmentation methods. As expected (see Fig. 3 and Supplementary Table S2), almost all measurements were larger than the real dimensions of the cylinders (Figs. 6 and 7).

Supplementary Table S3 contains the values of the diameter measurements in mm using the Frangi filter, the filtering method that has been most used in clinical research (Pham et al., 2022), to identify the cylinders of the physical phantom. The mean absolute differences between the real diameters and the measured ones for voxels of 0.3 mm-isotropic was 0.76 (SD=0.37, range=[0.2, 1.24]) mm. For voxels of 0.35 mm-isotropic it was the same but with range extending up to 1.27 mm. For voxels of 0.4 mm-isotropic the mean absolute differences were the highest: 0.81, (SD=0.39, range=[0.2, 1.31]) mm, and then declined for voxels of 0.45 mm-isotropic (0.78 (SD=0.35, range=[0.2, 1.27]) mm), to be the smallest (in average) for voxels of 0.5 mm-isotropic (0.62 (SD=0.24, range=[0.2, 0.96]) mm).

3.2. Effect of PVS orientation in measurements

Fig. 8 illustrates the diameters measured only on coronal orientation (upper row), and combining the measurements obtained from quantifying the cylinders placed (i.e., in the *in-silico* phantom) or scanned (i.e., in the UMC Utretch physical phantom) in different orientations. The true values slightly differ when the scan is acquired in a perpendicular or parallel plane to the cylinders with respect to those from when the images are acquired in oblique planes, but these differences were very small if the same image processing method (i.e., filter) was used (see Supplementary Fig. S3 and the dataset in https://doi.org/10.7488/ds/7454 for individual measurements and their average values in each orientation).

3.3. Influence of the Frangi filter parameters

A spatial resolution (i.e., voxel size) of 0.3 mm-isotropic was chosen to represent the effect of different values of α, β, c and scale parameters of the Frangi filter for the identification of the PVS-like structures. Alpha (α) controls the sensitivity of the filter in differentiating between tube-like and plate-like structures. Values of α that are too low allow more plate-like structures to be highlighted. As the length of the PVS of interest (i.e., the ones that are enlarged) ranges between 3 to 5 mm, $\alpha = 0.5$ was best suited to dismiss the smaller structures while increasing the sensitivity to distinguish elongated cylinders mimicking large PVS from wedge-like structures that could mimic typical lacunes (see results from α values of 0.1, 0.5 and 0.9 in Supplementary Fig. S4). Beta (β) controls the sensitivity of the filter in differentiating between tube-like and blob-like structures. Lower values of β reduce the sensitivity in detecting short cylinders and the filter response in the extremes of larger cylinders (Supplementary Fig. S5, left hand-side panel, $\beta = 0.1$). Values of β that are too high, allow more blob-like structures to be highlighted and cause a blob-like effect in the extremes of the cylinders (Supplementary Fig. S5, right hand-side panel, $\beta = 0.9$). The parameter *c* controls the sensitivity of the contrast between the bright/dark object (PVS) and the background (commonly normal-appearing brain tissue), but lower values of *c* could also increase false positives (see effects of values 50, 500 and 100 in Supplementary Fig. S6). The maximum scale parameter controls the sensitivity to the size of the cylinders. In principle, higher values of the maximum scale will detect bigger tubular objects (Supplementary Fig. S7), but it depends on the voxel size as well. Smaller voxel sizes require higher values compared with larger voxels to detect tubular structures of the same length. The scale ratio controls the sensitivity to detect cylinders of certain aspects' ratios, complementing the maximum scale parameter, but at a cost in computational time. Finer scales detect better the tubular structures but increase the computational time. Coarse scales would reduce the computational time but at the cost of not detecting some of these structures (Supplementary

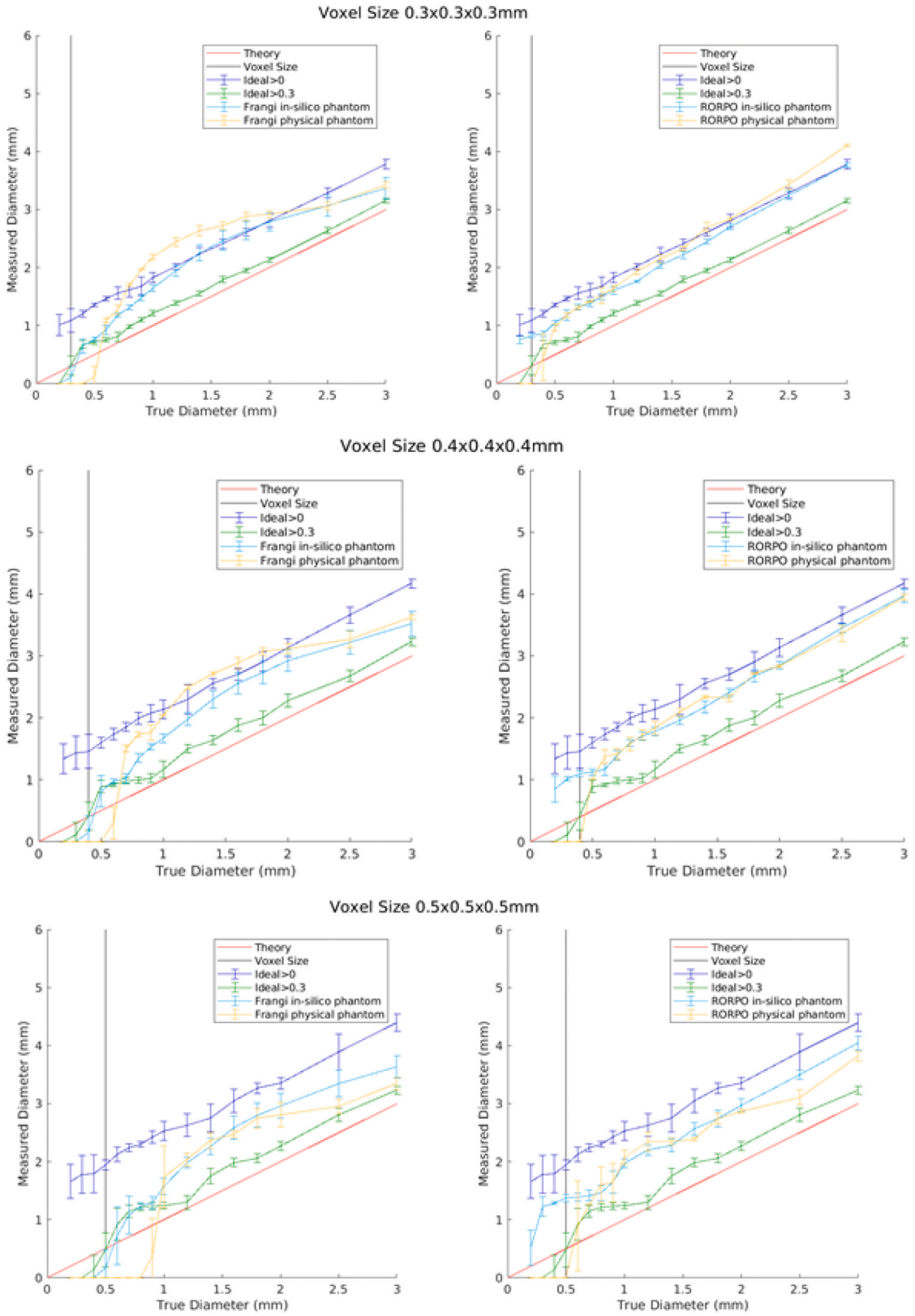

Fig. 6. Measurements of cylinder's diameters using the Frangi (left hand-side graphs) and RORPO (right hand-side graphs) filters for their detection in both phantoms, with isotropic voxel sizes of 0.3, 0.4 and 0.5 mm-isotropic and acquired resolutions equal to twice the reconstructed voxel sizes. The red line corresponds to the theoretically correct diameters (i.e., when the measured diameter is equal to the true diameter), the black line corresponds to the voxel size of the images, the dark blue line corresponds to the ideal segmentation of the *in-silico* phantom considering all voxels of the cylinders, the green line corresponds to the ideal segmentation of the in-silico phantom considering voxels located at least 30% inside the cylinders, the light blue line corresponds to the results for the in-silico phantom and the yellow line corresponds to the filter results for the physical phantom.

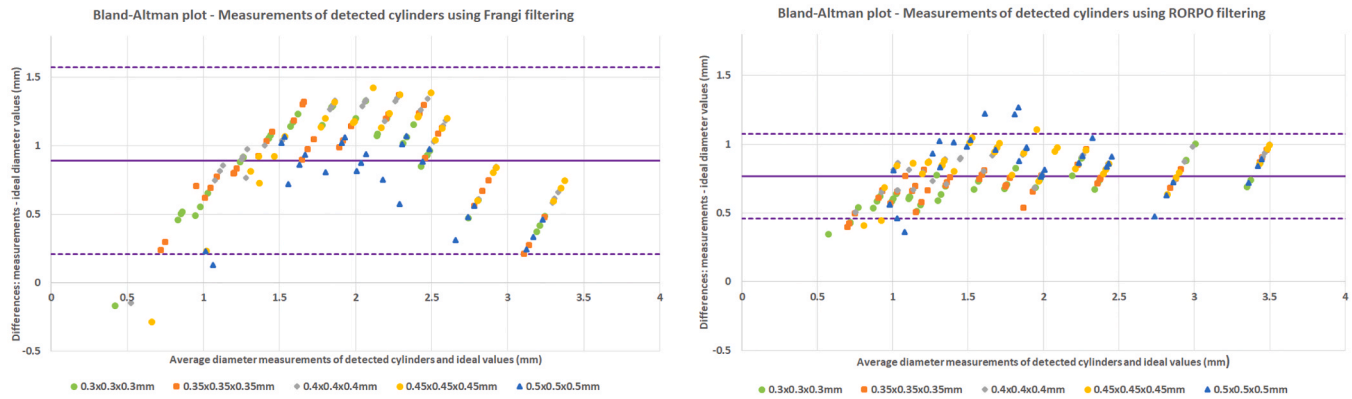

Fig. 7. Bland-Altman plots of the differences between the valid measurements from Frangi (left) and RORPO (right) at different voxel sizes (VS) and the real diameter of the cylinders of the physical phantom. Mean difference values for each voxel sizes are tabulated in Supplementary Table S5.

Fig. S8). Also, suboptimal scales can lead to either under or over-estimation of the size of the PVS. If there is over-estimation we could end up merging PVS that are close together altering the real count. Results from applying the Frangi filter to the physical phantom using different parameters, are shown in supplementary Figs. S10 to S13.

3.4. Influence of RORPO filter parameters

The RORPO filter only uses one parameter: the maximum scale representing the maximum length of the tubular objects to identify. Supplementary Fig. S9 illustrates the effect of this parameter for a spatial resolution of 0.3 mm-isotropic. In principle, higher values of the maximum scale will detect bigger tubular objects (Supplementary Fig. S9). The filter seems to be more sensitive to objects that are aligned to the Cartesian coordinates. The filter output inside the cylinders is more homogeneous than the output of the Frangi filter, thus explaining the more linear behaviour in Fig. 6. The impact of this parameter of the RORPO filter, in segmenting the water-filled cylinders of different diameters from the physical phantom at different voxel sizes, is illustrated in the Supplementary Fig. S14 for the S_{max} values of 18 and 46.

3.5. In-silico measurements in images with 1 mm^3 isotropic voxels

The limits in detecting cylinders of different diameters from both filters for voxels of 1 mm-isotropic can be seen in Fig. 9. With the given filter parameters and thresholds, the Frangi filter could detect cylinders with at least 2 mm of length and 1 mm diameter. The RORPO filter could detect narrower cylinders of 0.4 mm diameter.

Fig. 10 shows the length and diameter obtained from applying each filter with their optimal parameters. Cylinders (i.e., PVS-DROs) that did not have the minimum dimensions for being detected by each filter (as per results shown in Fig. 8) were removed from this analysis. Measurements with the Frangi filter were closer to the ideal segmentation of the in-silico phantom considering only voxels with at least 30% inside the cylinder, and overlapped with these ideal segmentations in length. Measurements using RORPO were closer to the ideal segmentation considering all voxels (i.e., either fully or partially) belonging to the cylinders. This can be explained by looking at the filters' output in the Supplementary Figs. S6-S7, RORPO filter output is more uniform across the whole cylinders that it detects, and in consequence the segmentation by thresholding will capture better the whole shape of the object. The Frangi filter, on the other hand, was better than RORPO in detecting the inner voxels of the cylinders rather than the boundary, which is rather confounded by partial volume effects. From these results we can confidently accept that a PVS grows in diameter and length if the change is at least twice the maximum standard deviation of the diameter regardless of the filtering method used. The maximum standard deviation of the diameter for the Frangi filter was 1.65 mm and for the RORPO filter it was 0.79 mm. RORPO lower standard deviation can be explained by the uniformity of the filter output throughout all diameters (Supplementary Fig. S9). Length measurements from using the Frangi filter were closer to the ideal segmentations (i.e., theoretical and considering voxels with at least 30% inside the cylinder) throughout the whole range analysed: 2 mm to 10 mm.

4. Discussion

4.1. Our contributions

We have developed and made publicly available an *in-silico* phantom using the PVS-DROs presented by Bernal et al. (2022), for testing and evaluating methods and MRI-acquisition protocols that allow to assess PVS-like fluid-filled small tubular structures. The use of the *in-silico* and physical phantoms presented here can provide useful information on the accuracy and detectability of structures that can be considered a proxy for PVS visible in MRI, not only for brain studies, but for the study of PVS in any other body organ, as well as any fluid-filled small tubular structure. They can also be used to assess precision and performance of other PVS computational analysis methods. The PVS-DRO model as used in our *in-silico* phantom can be tuned to agree with the spin-echo T2-weighted images of the UMC Utrecht physical phantom scanned in a 7 T Phillips scanner with different voxel sizes and different orientations. Both phantoms represent the tubular shape of PVS using cylinders for easiness in their representation and manipulation. A more sophisticated simulation can be achieved using Eq. (3) for the high-resolved image, and using the non-uniform Fourier transform to sample the *k*-space of the desired scan for simulating the low-resolution image. This would allow also to simulate more complex scenarios such as Rician-noise and ghosting, as per Bernal et al. (2022). We could define curved PVS using a parametric equation of the curved line and generating the PVS binary mask by setting to 1 all voxels that are inside the given radius of the PVS. However, such a representation would have introduced ambiguities in the interpretation of the results, as in such scenario a single "PVS" would had different orientations across its dimensionality.

4.2. Accuracy of the quantitative PVS measurements from MRI

The results presented show that in all cases, regardless of the filtering or image processing methods used, the boundaries of the PVS representation are consistently overestimated due to a) the fact that these structures do not cross the voxels by their centre (Supplementary Table 1) and b) partial volume effect (as seen in Fig. 3; and in Bernal et al., 2022). Therefore, as with many other MRI measures (Gassenmaier et al., 2020; Keenan et al., 2021; Illán-Gala et al., 2022; Nousiainen and Mäkelä, 2020), PVS measures from MRI are only a proxy of the true PVS

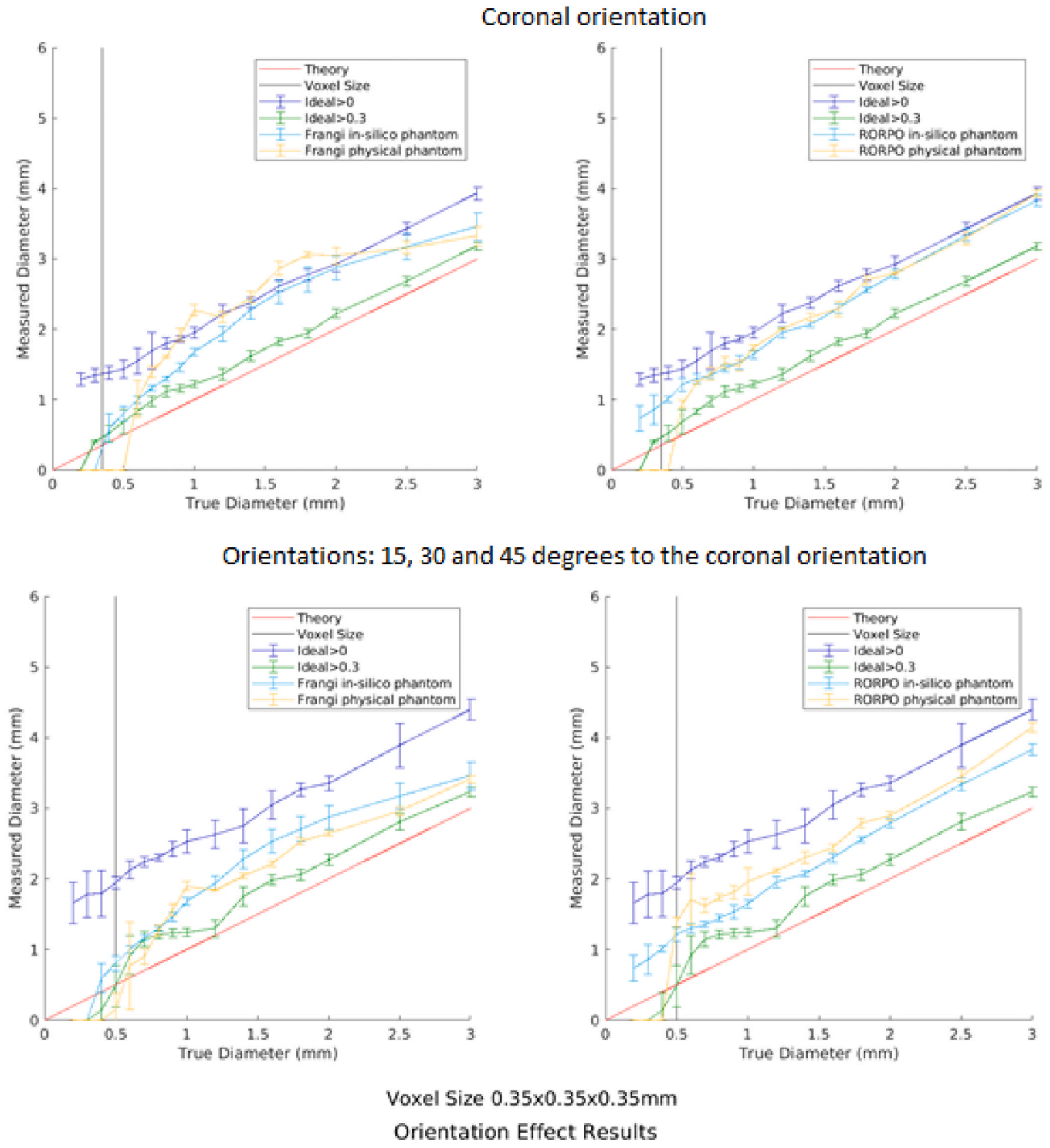

Fig. 8. Results of measuring the cylinders' (PVS-DROs') diameters in the *in-silico* and physical phantoms only in coronal orientation (upper row) and averaging the diameters' measurements from four different orientations: coronal, and 15°, 30° and 45° foot-head with respect to the coronal (bottom row) using the Frangi filter (left hand side plot) and RORPO (right hand side plot). The voxel size is $0.35 \times 0.35 \times 035$ mm^3 and the acquired resolution was equal to twice the reconstructed voxel size. The red line corresponds to the theoretically correct diameters (i.e., when the measured diameter is equal to the true diameter), the black line corresponds to the voxel size of the scans, the dark blue line corresponds to the ideal segmentation of the PVS-DROs considering all their voxels, the green line corresponds to the ideal segmentation of the PVS-DROs considering voxels located at least 30% inside them, the light blue line corresponds to the results for the *in-silico* phantom, and the yellow line correspond to the filter results for the physical phantom.

burden and individual dimensions, which depend on image resolution and processing methods, and which needs to be considered when comparing PVS measurements between scans.

4.3. *Influence of PVS orientation in the measurements' accuracy*

Our results suggest that PVS orientation is not an influential factor in differences between measurements. However, it must be noted that the

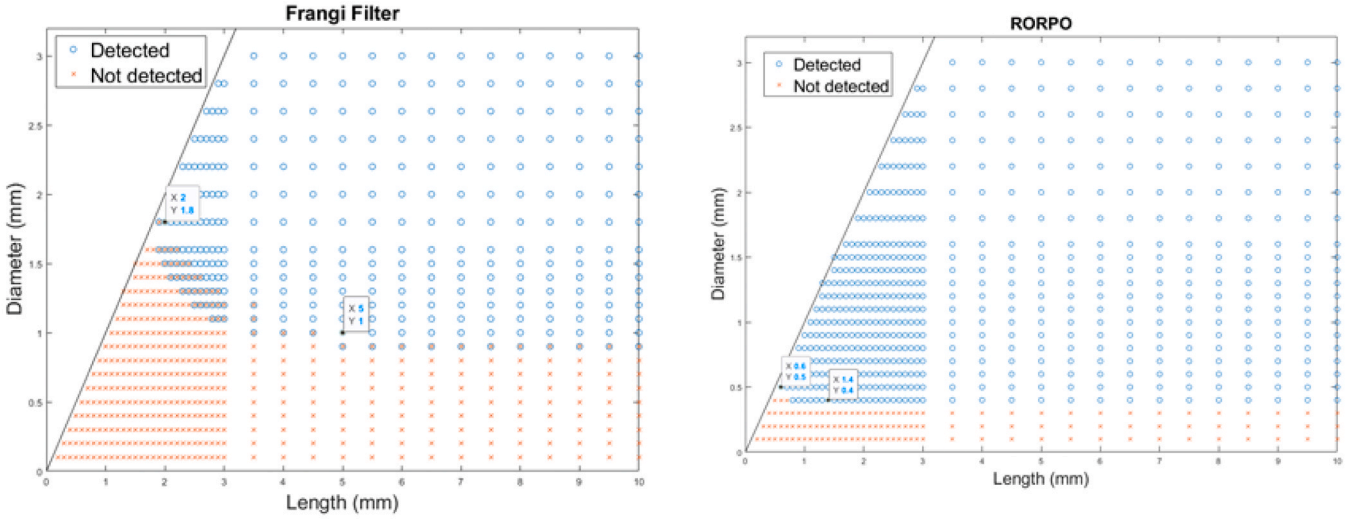

Fig. 9. Results from applying the Frangi (left) and RORPO (right) filters. Cylinders with diameter and lengths represented by the red crosses were not detected, whereas the ones represented by the blue circles were detected. Overlap in detection/not detection across the range of dimensions in the graphs is owed to the different spatial orientations of the cylinders. The cylinders with diameter greater than their length do not follow the definition of PVS and were not considered in the experiment.

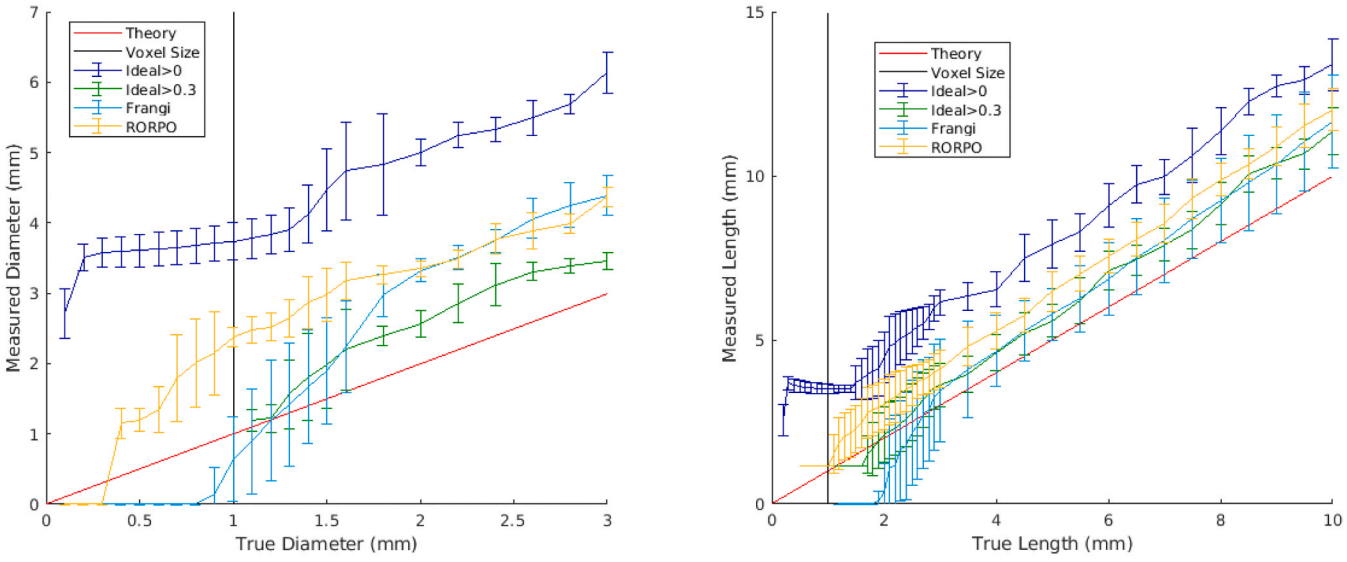

Fig. 10. Comparison of the computed diameters and lengths for both filters for the *in-silico* phantom of isotropic voxels of 1 mm^3. (Left) Diameters (Right) Lengths. The red line corresponds to the theoretically correct diameters/lengths (i.e., when the measured magnitude is equal to the true magnitude), the black line corresponds to the voxel size of the scans, the dark blue line corresponds to the ideal segmentation of the *in-silico* phantom considering voxel with any proportion of the cylinder, the green line corresponds to the ideal segmentation of the in-silico phantom considering voxels with at least 30% inside the cylinder, the light blue line corresponds to the Frangi filter results and the yellow line corresponds to the RORPO filter results.

use of the phantoms presented here with cylindrical DROs, but imaged with susceptibility-weighted sequences to represent blood-oxygen content in vessels would not yield the same conclusion. A study on the accuracy of MRI-based susceptibility measurements using also cylindrical objects reported variations in the observed induced fields as a function of the cylinders' orientation (Erdevig et al., 2017).

4.4. Frangi vs RORPO – recommendations on their use and limits of validity

The success in the use of the Frangi filter in detecting PVS-like structures from MRI relies on a careful tuning of several parameters. The combination of parameters proposed by Ballerini et al., (2016, 2018) $\alpha = 0.5$, $\beta = 0.5$ and c= 500 (although c may change depending on the signal intensity of the input image), proved to yield the best results in all the simulations done so far (i.e., here, and in Bernal et al., 2022), while the recommended scaling range and ratios may vary depending on the spatial resolution (i.e., voxel size) of the image and intensity contrast. RORPO, on the contrary, does not have these requirements, and compared with Frangi, allows detecting smaller cylinders in their entirety more accurately. The segmentation of the cylinders using the Frangi filter, however, seems to be best suited for voxel sizes equal or larger than 0.4 mm-isotropic and cylinders larger than 1 mm diameter and 2 mm length. Hence, although the use of the RORPO filter may seem to outperform that of the Frangi filter in most of the discussed scenarios, to establish either filter as a better choice, we need to analyse other factors such as voxel anisotropy, presence of Gibbs artefacts, Rician noise, curved PVS, presence of other imaging confounds as

lacunes and white matter hyperintensities, and grouping/clustering of PVS. Also, given that the PVS that are of interest clinically have larger sizes than the minimal dimensions for which Frangi seems to be best suited, in absence of artefacts or any confounding effects, the decision of whether to use one filtering method or the other comes down to the performance of the filter in the presence of these other factors.

4.5. Limitations

The phantoms have limitations in terms of their representation of the living brain. Importantly, they do not include the white matter hyperintensties, lacunes, varied background signal in normal-appearing white matter, etc., that are commonly associated with having more PVS. Therefore, a more realistic *in-silico* phantom mimicking spatial interaction of the tubular structures with other lesion-like features representatives of white matter hyperintensities, strokes and lacunes, will be needed to ascertain the influence of these confounds in the segmentation of PVS-like structures and evaluate the capability of the image-–processing methods to avoid false positives. While the discussed filters are designed to avoid objects that are not tube-like (e.g. blob-like and plate-like objects), the limits of these features needs to be further explored.

4.6. Future improvements

Although described as tubular structures, some PVS may interconnect forming vessel-like more complex structures or have a curvilinear shape. In these cases, building-upon more complex vessel phantoms (Gasser, 2012; Gholami Bajestani et al., 2022) would be beneficial to ascertain the performance of current algorithms in such scenarios. In such cases, PVS morphometrics may not be accurately calculated using the ellipsoid approximation model implemented by the pegionprops3 function in MATLAB, used here. The use of a cubic Bézier curve approximation model instead seems promising in such scenarios (Duarte Coello et al., 2023).

Although deep learning methods are still to be established for PVS-segmentations, promising results of experimental schemes have been emerging (Pham et al., 2022; Barisano et al., 2022). Further evaluation of these architectures using the phantoms presented here will hopefully help in the standardisation of the PVS segmentation with views at cross-studies analyses to advance the knowledge about the role of these structures in brain health.

CRediT authorship contribution statement

Moyano José Bernal: Writing – review & editing, Validation, Software, Methodology, Investigation, Formal analysis, Data curation, Conceptualization. **Ballerini Lucia:** Writing – review & editing, Validation, Software, Methodology, Investigation, Conceptualization. **Kuijf Hugo J.:** Writing – review & editing, Supervision, Resources, Project administration, Methodology, Investigation, Funding acquisition, Formal analysis, Conceptualization. **De Luca Alberto:** Writing – review & editing, Visualization, Validation, Data curation. **Biessels Geert Jan:** Writing – review & editing, Supervision, Resources, Project administration, Methodology, Funding acquisition. **Coello Roberto Duarte:** Writing – review & editing, Visualization, Validation, Software, Methodology, Investigation, Formal analysis, Data curation, Conceptualization. **Chappell Francesca M.:** Writing – review & editing, Validation, Supervision, Methodology, Data curation. **Brown Rosalind:** Writing – review & editing, Validation, Resources, Project administration. **Zwanenburg Jaco J.M.:** Writing – review & editing, Visualization, Validation, Supervision, Resources, Methodology, Conceptualization. **van der Velden Moniek:** Writing – review & editing, Visualization, Validation, Software, Investigation, Formal analysis, Data curation. **Wardlaw Joanna M.:** Writing – review & editing, Validation, Supervision, Resources, Project administration, Methodology, Investigation, Funding acquisition, Conceptualization. **Valdés Hernández Maria C.:** Writing – original draft, Visualization, Validation, Supervision, Software, Methodology, Investigation, Formal analysis, Conceptualization.

Declaration of Competing Interest

Authors declare no competing interests.

Data availability

Data has been made publicly available and the link to access it is provided in the manuscript.

Acknowledgements

We thank Dr. Michael Thrippleton for a useful discussion and insights in evaluating the geometric distortions of the physical phantom. This study is mainly funded by the Hilary and Galen Weston Foundation under the Novel Biomarkers 2019 scheme (ref UB190097) administered by the Weston Brain Institute. This study received also funds from the Fondation Leducq Network of Excellence for the Study of Perivascular Spaces in Small Vessel Disease (16 CVD 05); the MRC Doctoral Training Programme in Precision Medicine (JB); the Row Fogo Charitable Trust (MCVH, FC) (BRO-D.FID3668413); and the UK Dementia Research Institute at the University of Edinburgh funded by the Medical Research Council, Alzheimer's Society and Alzheimer's Research UK (JMW).

Appendix A. Supporting information

Supplementary data associated with this article can be found in the online version at doi:10.1016/j.jneumeth.2023.110039.

References

Aribisala, B.S., Wiseman, S., Morris, Z., Valdés-Hernández, M.C., Royle, N.A., Maniega, S. M., Gow, A.J., Corley, J., Bastin, M.E., Starr, J., Deary, I.J., Wardlaw, J.M., 2014. Circulating inflammatory markers are associated with magnetic resonance imaging-visible perivascular spaces but not directly with white matter hyperintensities. Stroke 45 (2), 605–607. https://doi.org/10.1161/STROKEAHA.113.004059.

Aribisala, B.S., Riha, R.L., Valdes Hernandez, M., Muñoz Maniega, S., Cox, S., Radakovic, R., Taylor, A., Pattie, A., Corley, J., Redmond, P., Bastin, M.E., Starr, J., Deary, I., Wardlaw, J.M., 2020. Sleep and brain morphological changes in the eighth decade of life. Sleep. Med. 65, 152–158. https://doi.org/10.1016/j.sleep.2019.07.015.

Aribisala, B.S., Valdés Hernández, M.D.C., Okely, J.A., Cox, S.R., Ballerini, L., Dickie, D. A., Wiseman, S.J., Riha, R.L., Muñoz Maniega, S., Radakovic, R., Taylor, A., Pattie, A., Corley, J., Redmond, P., Bastin, M.E., Deary, I., Wardlaw, J.M., 2023. Sleep quality, perivascular spaces and brain health markers in ageing - a longitudinal study in the Lothian Birth Cohort 1936. Sleep Med. 106, 123–131. https://doi.org/10.1016/j.sleep.2023.03.016.

Ballerini, L., Lovreglio, R., Valdés Hernández, M.D.C., Gonzalez-Castro, V., Muñoz Maniega, S., Pellegrini, E., Bastin, M.E., Deary, I.J., Wardlaw, J.M., 2016. Application of the ordered logit model to optimising frangi filter parameters for segmentation of perivascular spaces. Procedia Comput. Sci. 90, 61–67. https://doi.org/10.1016/j.procs.2016.07.011.

Ballerini, L., Lovreglio, R., Valdés Hernández, M.D.C., Ramirez, J., MacIntosh, B.J., Black, S.E., Wardlaw, J.M., 2018. Perivascular spaces segmentation in brain MRI using optimal 3D filtering. Sci. Rep. 8 (1), 11. https://doi.org/10.1038/s41598-018-19781-5.

Baril, A.A., Pinheiro, A.A., Himali, J.J., Beiser, A., Sanchez, E., Pase, M.P., Seshadri, S., Demissie, S., Romero, J.R., 2022. Lighter sleep is associated with higher enlarged perivascular spaces burden in middle-aged and elderly individuals. Sleep Med. 100, 558–564. https://doi.org/10.1016/j.sleep.2022.10.006.

Barisano, G., Lynch, K.M., Sibilia, F., Lan, H., Shih, N.C., Sepehrband, F., Choupan, J., 2022. Imaging perivascular space structure and function using brain MRI. Neuroimage 257, 119329. https://doi.org/10.1016/j.neuroimage.2022.119329.

Berezuk, C., Ramirez, J., Gao, F., Scott, C.J., Huroy, M., Swartz, R.H., Murray, B.J., Black, S.E., Boulos, M.I., 2015. Virchow-Robin spaces: correlations with polysomnography-derived sleep parameters. Sleep 38 (6), 853–858. https://doi.org/10.5665/sleep.4726.

Bernal, J., Valdés-Hernández, M.D.C., Escudero, J., Duarte, R., Ballerini, L., Bastin, M.E., Deary, I.J., Thrippleton, M.J., Touyz, R.M., Wardlaw, J.M., 2022. Assessment of perivascular space filtering methods using a three-dimensional computational model. Magn. Reson. Imaging 93, 33–51. https://doi.org/10.1016/j.mri.2022.07.016.

Bouvy, W.H., Biessels, G.J., Kuijf, H.J., Kappelle, L.J., Luijten, P.R., Zwanenburg, J.J., 2014. Visualization of perivascular spaces and perforating arteries with 7 T magnetic resonance imaging. Investig. Radiol. 49 (5), 307–313. https://doi.org/10.1097/RLI.0000000000000027.

Del Brutto, O.H., Mera, R.M., Del Brutto, V.J., Castillo, P.R., 2019. Enlarged basal ganglia perivascular spaces and sleep parameters. A population-based study. Clin. Neurol. Neurosurg. 182, 53–57. https://doi.org/10.1016/j.clineuro.2019.05.002.

Donahue, E.K., Murdos, A., Jakowec, M.W., Sheikh-Bahaei, N., Toga, A.W., petzinger, G. M., Sepehrband, F., 2021. Global and regional changes in perivascular space in idiopathic and familial Parkinson's disease. Mov. Disord. 28473. https://doi.org/10.1002/mds.28473.

Duarte Coello, R., Valdés Hernández, M.C., Ballerini, L., Bernal Moyano, J., Chappell, F. M., Brown, R., Wardlaw, J.M., Zwanenburg, J., Van Der Velden, M., Kuijf, H.J., 2023. Measurements of a perivascular spaces magnetic resonance imaging physical phantom and correspondent digital reference object model, 2023 [dataset]. University of Edinburgh. Centre for Clinical Brain Sciences. Dep. Neuroimaging Sci. https://doi.org/10.7488/ds/7454.

Dubost, F., Yilmaz, P., Adams, H., Bortsova, G., Ikram, M.A., Niessen, W., Vernooij, M., de Bruijne, M., 2019. Enlarged perivascular spaces in brain MRI: Automated quantification in four regions. Neuroimage 185, 534–544. https://doi.org/10.1016/j.neuroimage.2018.10.026.

Erdevig, H., Russek, S., Carnicka, S., Stupic, K., Keenan, K., 2017. Accuracy of magnetic resonance based susceptibility measurements. AIP Adv. ⟨https://tsapps.nist.gov/publication/get_pdf.cfm?pub_id=921907⟩ Accessed October 18, 2023.

Francis, F., Ballerini, L., Wardlaw, J.M., 2019. Perivascular spaces and their associations with risk factors, clinical disorders and neuroimaging features: a systematic review and meta-analysis. Int J. Stroke 14 (4), 359–371. https://doi.org/10.1177/1747493019830321.

Frangi, A.F., Niessen, W.J., Vincken, K.L., Viergever, M.A., 1998. Multiscale vessel enhancement filtering 130–137. https://doi.org/10.1007/BFb0056195.

Gassenmaier, S., Tsiflikas, I., Maennlin, S., et al., 2020. Retrospective accuracy analysis of MRI based lesion size measurement in neuroblastic tumors: which sequence should we choose? BMC Med. Imaging 20, 105. https://doi.org/10.1186/s12880-020-00503-1.

Gasser, T.C., 2012. Bringing vascular biomechanics into clinical practice. Simulation-based decisions for elective abdominal aortic aneurysms repair. In: Calvo Lopez, B., Peña, E. (Eds.), Patient-Specific Computational Modeling. Lecture Notes in Computational Vision and Biomechanics, vol 5. Springer, Dordrecht. https://doi.org/10.1007/978-94-007-4552-0_1.

Gholami Bajestani, D., Reich, C.M., Mulik, C., Mokosch, M., Melzer, A., 2022. Hybrid polymer vessel phantoms for feasibility studies and clinical training of MRI-guided interventions. Curr. Dir. Biomed. Eng. 8 (2), 656–659. https://doi.org/10.1515/cdbme-2022-1167.

Hilal, S., Tan, C.S., Adams, H.H.H., Habes, M., Mok, V., Venketasubramanian, N., Hofer, E., Ikram, M.K., Abrigo, J., Vernooij, M.W., Chen, C., Hosten, N., Volzke, H., Grabe, H.J., Schmidt, R., Ikram, M.A., 2018. Enlarged perivascular spaces and cognition: a meta-analysis of 5 population-based studies. Neurology 91 (9), e832–e842. https://doi.org/10.1212/WNL.0000000000006079.

Illán-Gala, I., Nigro, S., Vande Vrede, L., Falgàs, N., Heuer, H.W., Painous, C., Compta, Y., Martí, M.J., Montal, V., Pagonabarraga, J., Kulisevsky, J., Lleó, A., Fortea, J., Logroscino, G., Quattrone, A., Perry, D.C., Gorno-Tempini, M.L., Rosen, H.J., Grinberg, L.T., Spina, S., La Joie, R., Rabinovici, G.D., Miller, B.L., Rojas, J.C., Seeley, W.W., Boxer, A.L., 2022. Diagnostic accuracy of magnetic resonance imaging measures of brain atrophy across the spectrum of progressive supranuclear palsy and corticobasal degeneration. JAMA Netw. Open 5 (4), e229588. ⟨https://doi.org/10.1001/jamanetworkopen.2022.9588⟩. Erratum in: JAMA Netw Open. 2022 May 2;5 (5), e2217977.

Jerman, T.; Pemuš, F.; Likar, B.; Špiclin, Ž., 2015. Beyond Frangi: an improved multiscale vesselness filter. Proceedings Volume 9413, Medical Imaging 2015: Image Processing; 94132A https://doi.org/10.1117/12.2081147.

Keenan, K.E., Gimbutas, Z., Dienstfrey, A., Stupic, K.F., Boss, M.A., Russek, S.E., Chenevert, T.L., Prasad, P.V., Guo, J., Reddick, W.E., Cecil, K.M., Shukla-Dave, A., Aramburu Nunez, D., Shridhar Konar, A., Liu, M.Z., Jambawalikar, S.R., Schwartz, L. H., Zheng, J., Hu, P., Jackson, E.F., 2021. Multi-site, multi-platform comparison of MRI T1 measurement using the system phantom. PLOS One 16 (6), e0252966. https://doi.org/10.1371/journal.pone.0252966.

Lerski, R.A., de Wilde, J., Boyce, D., Ridgeway, J., 1998. Quality Control in Magnetic Resonance Imaging, IPEM Report 80. The Institute of Physics and Engineering in Medicine,, York.

Merveille, O., Talbot, H., Najman, L., Passat, N., 2018. Curvilinear structure analysis by ranking the orientation responses of path operators. IEEE Trans. Pattern Anal. Mach. Intell. 40, 304–317. https://doi.org/10.1109/TPAMI.2017.2672972.

Nousiainen, K., Mäkelä, T., 2020. Measuring geometric accuracy in magnetic resonance imaging with 3D-printed phantom and nonrigid image registration. Magn. Reson Mater. Phys. 33, 401–410. https://doi.org/10.1007/s10334-019-00788-6.

Passiak, B.S., Liu, D., Kresge, H.A., Cambronero, F.E., Pechman, K.R., Osborn, K.E., Gifford, K.A., Hohman, T.J., Schrag, M.S., Davis, L.T., Jefferson, A.L., 2019. Perivascular spaces contribute to cognition beyond other small vessel disease markers. Neurology 92 (12), e1309–e1321. https://doi.org/10.1212/WNL.0000000000007124.

Patankar, T.F., Mitra, D., Varma, A., Snowden, J., Neary, D., Jackson, A., 2005. Dilatation of the Virchow-Robin space is a sensitive indicator of cerebral microvascular disease: study in elderly patients with dementia. AJNR Am. J. Neuroradiol. 26 (6), 1512–1520.

Pham, W., Lynch, M., Spitz, G., O'Brien, T., Vivash, L., Sinclair, B., Law, M., 2022. A critical guide to the automated quantification of perivascular spaces in magnetic resonance imaging. Front. Neurosci. 16, 1021311 https://doi.org/10.3389/fnins.2022.1021311.

Potter, G.M., Doubal, F.N., Jackson, C.A., Chappell, F.M., Sudlow, C.L., Dennis, M.S., Wardlaw, J.M., 2015. Enlarged perivascular spaces and cerebral small vessel disease. Int. J. Stroke 10 (3), 376–381. https://doi.org/10.1111/ijs.12054.

Price, R.R., Axel, L., Morgan, T., Newman, R., Perman, W., Schneiders, N., Selikson, M., Wood, M., Thomas, S.R., 1990. Quality assurance methods and phantoms for magnetic resonance imaging: report of AAPM nuclear magnetic resonance Task Group No. 1. Med, Phys. 17 (2), 287–295. https://doi.org/10.1118/1.596566.

Sepehrband, F., Barisano, G., Sheikh-Bahaei, N., Choupan, J., Cabeen, R.P., Lynch, K.M., Crawford, M.S., Lan, H., Mack, W.J., Chu,i, H.C., Ringman, J.M., Toga, A.W., 2021. Alzheimer's disease neuroimaging initiative. Volumetric distribution of perivascular space in relation to mild cognitive impairment. Neurobiol. Aging 99, 28–43. https://doi.org/10.1016/j.neurobiolaging.2020.12.010.

Valdés Hernández, M. del C., Piper, R.J., Wang, X., Deary, I.J., Wardlaw, J.M., 2013. Towards the automatic computational assessment of enlarged perivascular spaces on brain magnetic resonance images: a systematic review. J. Magn. Reson. Imaging 38, 774–785. https://doi.org/10.1002/jmri.24047.

Wang, D., Doddrell, D.M., 2005. Geometric distortion in structural magnetic resonance imaging. Curr. Med. Imag. Rev. 1, 49–60.

Wardlaw, J.M., Smith, E.E., Biessels, G.J., Cordonnier, C., Fazekas, F., Frayne, R., Lindley, R.I., O'Brien, J.T., Barkhof, F., Benavente, O.R., Black, S.E., Brayne, C., Breteler, M., Chabriat, H., DeCarli, C., de Leeuw, F.E., Doubal, F., Duering, M., Fox, N.C., Greenberg, S., Hachinski, V., Kilimann, I., Mok, V., Oostenbrugge, R., van, Pantoni, L., Speck, O., Stephan, B.C.M., Teipel, S., Viswanathan, A., Werring, D., Chen, C., Smith, C., van Buchem, M., Norrving, B., Gorelick, P.B., Dichgans, M., 2013. Neuroimaging standards for research into small vessel disease and its contribution to ageing and neurodegeneration. Lancet Neurol. 12, 822–838. https://doi.org/10.1016/S1474-4422(13)70124-8.

Wardlaw, J.M., Benveniste, H., Nedergaard, M., Zlokovic, B.V., Mestre, H., Lee, H., Douba,l, F.N., Brown, R., Ramirez, J., Macintosh, B.J., et al., 2020. Perivascular spaces in the brain: anatomy, physiology and pathology. Nat. Rev. Neurol. 16, 137–153.